

Observation of a vector charmoniumlike state in $e^+e^- \rightarrow D_s^+ D_{s1}^-(2536)^- + c.c.$

S. Jia,² C. P. Shen,⁹ C. Z. Yuan,²⁴ X. L. Wang,⁹ I. Adachi,^{15,11} H. Aihara,⁸³ D. M. Asner,³ H. Atmacan,⁷⁵ V. Aulchenko,^{4,64} R. Ayad,⁷⁸ V. Babu,⁸ I. Badhrees,^{78,33} A. M. Bakich,⁷⁷ P. Behera,²² B. Bhuyan,²⁰ T. Bilka,⁵ J. Biswal,³⁰ A. Bobrov,^{4,64} G. Bonvicini,⁸⁷ A. Bozek,⁶⁰ M. Bračko,^{46,30} T. E. Browder,¹⁴ M. Campajola,^{27,55} L. Cao,³¹ D. Červenkov,⁵ P. Chang,⁵⁹ A. Chen,⁵⁷ B. G. Cheon,¹³ K. Chilikin,⁴⁰ H. E. Cho,¹³ K. Cho,³⁴ S.-K. Choi,¹² Y. Choi,⁷⁶ D. Cinabro,⁸⁷ S. Cunliffe,⁸ G. De Nardo,^{27,55} F. Di Capua,^{27,55} S. Di Carlo,³⁸ Z. Doležal,⁵ T. V. Dong,⁹ S. Eidelman,^{4,64,40} D. Epifanov,^{4,64} J. E. Fast,⁶⁶ T. Ferber,⁸ B. G. Fulsom,⁶⁶ R. Garg,⁶⁷ V. Gaur,⁸⁶ N. Gabyshev,^{4,64} A. Garmash,^{4,64} A. Giri,²¹ P. Goldenzweig,³¹ B. Golob,^{42,30} K. Hayasaka,⁶² H. Hayashii,⁵⁶ W.-S. Hou,⁵⁹ C.-L. Hsu,⁷⁷ T. Iijima,^{54,53} K. Inami,⁵³ G. Inguglia,²⁵ A. Ishikawa,^{15,11} R. Itoh,^{15,11} M. Iwasaki,⁶⁵ Y. Iwasaki,¹⁵ W. W. Jacobs,²³ Y. Jin,⁸³ K. K. Joo,⁶ K. H. Kang,³⁷ G. Karyan,⁸ H. Kichimi,¹⁵ B. H. Kim,⁷² C. H. Kim,¹³ D. Y. Kim,⁷⁴ S. H. Kim,¹³ K. Kinoshita,⁷ P. Kodyš,⁵ S. Korpar,^{46,30} R. Kroeger,⁴⁹ P. Krokovny,^{4,64} R. Kulasiri,³² A. Kuzmin,^{4,64} Y.-J. Kwon,⁸⁹ K. Lalwani,⁴⁵ J. S. Lange,¹⁰ I. S. Lee,¹³ S. C. Lee,³⁷ P. Lewis,¹⁴ C. H. Li,⁴¹ L. K. Li,²⁴ Y. B. Li,⁶⁸ L. Li Gioi,⁴⁷ J. Libby,²² K. Lieret,⁴³ D. Liventsev,^{86,15} C. MacQueen,⁴⁸ M. Masuda,⁸² T. Matsuda,⁵⁰ D. Matvienko,^{4,64,40} M. Merola,^{27,55} K. Miyabayashi,⁵⁶ H. Miyata,⁶² R. Mizuk,^{40,52} R. Mussa,²⁸ K. J. Nath,²⁰ M. Nayak,^{87,15} M. Niiyama,³⁶ N. K. Nisar,⁶⁹ S. Nishida,^{15,11} K. Nishimura,¹⁴ S. Ogawa,⁸¹ H. Ono,^{61,62} Y. Onuki,⁸³ P. Oskin,⁴⁰ P. Pakhlov,^{40,51} G. Pakhlova,^{40,52} T. Pang,⁶⁹ S. Pardi,²⁷ H. Park,³⁷ S.-H. Park,⁸⁹ S. Patra,¹⁹ S. Paul,⁸⁰ T. K. Pedlar,⁴⁴ R. Pestotnik,³⁰ L. E. Piilonen,⁸⁶ V. Popov,^{40,52} E. Prencipe,¹⁷ M. T. Prim,³¹ M. Röhrken,⁸ A. Rostomyan,⁸ N. Rout,²² G. Russo,⁵⁵ D. Sahoo,⁷⁹ Y. Sakai,^{15,11} S. Sandilya,⁷ L. Santelj,¹⁵ V. Savinov,⁶⁹ O. Schneider,³⁹ G. Schnell,^{1,18} C. Schwanda,²⁵ Y. Seino,⁶² K. Senyo,⁸⁸ M. E. Sevier,⁴⁸ J.-G. Shiu,⁵⁹ B. Shwartz,^{4,64} A. Sokolov,²⁶ E. Solovieva,⁴⁰ S. Stanič,⁶³ M. Starič,³⁰ Z. S. Stottler,⁸⁶ T. Sumiyoshi,⁸⁵ W. Sutcliffe,³¹ M. Takizawa,^{73,16,70} K. Tanida,²⁹ F. Tenchini,⁸ K. Trabelsi,³⁸ M. Uchida,⁸⁴ T. Uglov,^{40,52} Y. Unno,¹³ S. Uno,^{15,11} Y. Usov,^{4,64} R. Van Tonder,³¹ G. Varner,¹⁴ A. Vinokurova,^{4,64} V. Vorobyev,^{4,64,40} C. H. Wang,⁵⁸ M.-Z. Wang,⁵⁹ M. Watanabe,⁶² E. Won,³⁵ S. B. Yang,³⁵ H. Ye,⁸ J. H. Yin,²⁴ Z. P. Zhang,⁷¹ V. Zhilich,^{4,64} V. Zhukova,⁴⁰ and V. Zhulanov^{4,64}

(The Belle Collaboration)

¹University of the Basque Country UPV/EHU, 48080 Bilbao

²Beihang University, Beijing 100191

³Brookhaven National Laboratory, Upton, New York 11973

⁴Budker Institute of Nuclear Physics SB RAS, Novosibirsk 630090

⁵Faculty of Mathematics and Physics, Charles University, 121 16 Prague

⁶Chonnam National University, Gwangju 61186

⁷University of Cincinnati, Cincinnati, Ohio 45221

⁸Deutsches Elektronen-Synchrotron, 22607 Hamburg

⁹Key Laboratory of Nuclear Physics and Ion-beam Application (MOE) and Institute of Modern Physics, Fudan University, Shanghai 200443

¹⁰Justus-Liebig-Universität Gießen, 35392 Gießen

¹¹SOKENDAI (The Graduate University for Advanced Studies), Hayama 240-0193

¹²Gyeongsang National University, Jinju 52828

¹³Department of Physics and Institute of Natural Sciences, Hanyang University, Seoul 04763

¹⁴University of Hawaii, Honolulu, Hawaii 96822

¹⁵High Energy Accelerator Research Organization (KEK), Tsukuba 305-0801

¹⁶J-PARC Branch, KEK Theory Center, High Energy Accelerator Research Organization (KEK), Tsukuba 305-0801

¹⁷Forschungszentrum Jülich, 52425 Jülich

¹⁸IKERBASQUE, Basque Foundation for Science, 48013 Bilbao

¹⁹Indian Institute of Science Education and Research Mohali, SAS Nagar, 140306

²⁰Indian Institute of Technology Guwahati, Assam 781039

²¹Indian Institute of Technology Hyderabad, Telangana 502285

- ²²Indian Institute of Technology Madras, Chennai 600036
- ²³Indiana University, Bloomington, Indiana 47408
- ²⁴Institute of High Energy Physics, Chinese Academy of Sciences, Beijing 100049
- ²⁵Institute of High Energy Physics, Vienna 1050
- ²⁶Institute for High Energy Physics, Protvino 142281
- ²⁷INFN - Sezione di Napoli, 80126 Napoli
- ²⁸INFN - Sezione di Torino, 10125 Torino
- ²⁹Advanced Science Research Center, Japan Atomic Energy Agency, Naka 319-1195
- ³⁰J. Stefan Institute, 1000 Ljubljana
- ³¹Institut für Experimentelle Teilchenphysik, Karlsruher Institut für Technologie, 76131 Karlsruhe
- ³²Kennesaw State University, Kennesaw, Georgia 30144
- ³³King Abdulaziz City for Science and Technology, Riyadh 11442
- ³⁴Korea Institute of Science and Technology Information, Daejeon 34141
- ³⁵Korea University, Seoul 02841
- ³⁶Kyoto University, Kyoto 606-8502
- ³⁷Kyungpook National University, Daegu 41566
- ³⁸LAL, Univ. Paris-Sud, CNRS/IN2P3, Université Paris-Saclay, Orsay 91898
- ³⁹École Polytechnique Fédérale de Lausanne (EPFL), Lausanne 1015
- ⁴⁰P.N. Lebedev Physical Institute of the Russian Academy of Sciences, Moscow 119991
- ⁴¹Liaoning Normal University, Dalian 116029
- ⁴²Faculty of Mathematics and Physics, University of Ljubljana, 1000 Ljubljana
- ⁴³Ludwig Maximilians University, 80539 Munich
- ⁴⁴Luther College, Decorah, Iowa 52101
- ⁴⁵Malaviya National Institute of Technology Jaipur, Jaipur 302017
- ⁴⁶University of Maribor, 2000 Maribor
- ⁴⁷Max-Planck-Institut für Physik, 80805 München
- ⁴⁸School of Physics, University of Melbourne, Victoria 3010
- ⁴⁹University of Mississippi, University, Mississippi 38677
- ⁵⁰University of Miyazaki, Miyazaki 889-2192
- ⁵¹Moscow Physical Engineering Institute, Moscow 115409
- ⁵²Moscow Institute of Physics and Technology, Moscow Region 141700
- ⁵³Graduate School of Science, Nagoya University, Nagoya 464-8602
- ⁵⁴Kobayashi-Maskawa Institute, Nagoya University, Nagoya 464-8602
- ⁵⁵Università di Napoli Federico II, 80055 Napoli
- ⁵⁶Nara Women's University, Nara 630-8506
- ⁵⁷National Central University, Chung-li 32054
- ⁵⁸National United University, Miao Li 36003
- ⁵⁹Department of Physics, National Taiwan University, Taipei 10617
- ⁶⁰H. Niewodniczanski Institute of Nuclear Physics, Krakow 31-342
- ⁶¹Nippon Dental University, Niigata 951-8580
- ⁶²Niigata University, Niigata 950-2181
- ⁶³University of Nova Gorica, 5000 Nova Gorica
- ⁶⁴Novosibirsk State University, Novosibirsk 630090
- ⁶⁵Osaka City University, Osaka 558-8585

⁶⁶*Pacific Northwest National Laboratory, Richland, Washington 99352*

⁶⁷*Panjab University, Chandigarh 160014*

⁶⁸*Peking University, Beijing 100871*

⁶⁹*University of Pittsburgh, Pittsburgh, Pennsylvania 15260*

⁷⁰*Theoretical Research Division, Nishina Center, RIKEN, Saitama 351-0198*

⁷¹*University of Science and Technology of China, Hefei 230026*

⁷²*Seoul National University, Seoul 08826*

⁷³*Showa Pharmaceutical University, Tokyo 194-8543*

⁷⁴*Soongsil University, Seoul 06978*

⁷⁵*University of South Carolina, Columbia, South Carolina 29208*

⁷⁶*Sungkyunkwan University, Suwon 16419*

⁷⁷*School of Physics, University of Sydney, New South Wales 2006*

⁷⁸*Department of Physics, Faculty of Science, University of Tabuk, Tabuk 71451*

⁷⁹*Tata Institute of Fundamental Research, Mumbai 400005*

⁸⁰*Department of Physics, Technische Universität München, 85748 Garching*

⁸¹*Toho University, Funabashi 274-8510*

⁸²*Earthquake Research Institute, University of Tokyo, Tokyo 113-0032*

⁸³*Department of Physics, University of Tokyo, Tokyo 113-0033*

⁸⁴*Tokyo Institute of Technology, Tokyo 152-8550*

⁸⁵*Tokyo Metropolitan University, Tokyo 192-0397*

⁸⁶*Virginia Polytechnic Institute and State University, Blacksburg, Virginia 24061*

⁸⁷*Wayne State University, Detroit, Michigan 48202*

⁸⁸*Yamagata University, Yamagata 990-8560*

⁸⁹*Yonsei University, Seoul 03722*

Using a data sample of 921.9 fb^{-1} collected with the Belle detector, we study the process of $e^+e^- \rightarrow D_s^+ D_{s1}(2536)^- + c.c.$ via initial-state radiation. We report the first observation of a vector charmoniumlike state decaying to $D_s^+ D_{s1}(2536)^- + c.c.$ with a significance of 5.9σ , including the systematic uncertainties. The measured mass and width are $(4625.9_{-6.0}^{+6.2}(\text{stat.}) \pm 0.4(\text{syst.})) \text{ MeV}/c^2$ and $(49.8_{-11.5}^{+13.9}(\text{stat.}) \pm 4.0(\text{syst.})) \text{ MeV}$, respectively. The product of the $e^+e^- \rightarrow D_s^+ D_{s1}(2536)^- + c.c.$ cross section and the branching fraction of $D_{s1}(2536)^- \rightarrow \bar{D}^{*0} K^-$ is measured from the $D_s \bar{D}_{s1}(2536)$ threshold to 5.59 GeV .

PACS numbers: 13.66.Bc, 13.87.Fh, 14.40.Lb

In the past decade, measurements of the exclusive cross sections for e^+e^- annihilation into charmed or charmed-strange meson pairs and charmed baryon pairs above the open-charm threshold have attracted much attention [1–11]. Unexpected strong near-threshold enhancements are present in the $e^+e^- \rightarrow D\bar{D}$, $D^{(*)+}D^{*-}$, $D_s^+D_s^-$, and $\Lambda_c^+\bar{\Lambda}_c^-$ cross sections [1, 2, 5–7]. These open-charm final states are dominantly produced from the OZI-allowed strong decays of excited vector charmonium states (ψ states). Due to the lack of adequate experimental measurements and sophisticated theoretical models, the couplings of these ψ states to the open-charm final states as well as the resonant parameters of these charmonium states are not well measured.

Many additional Y states with $J^{PC} = 1^{--}$ lying with

masses above the open-charm threshold have been discovered in the last 14 years [12–20]. In $e^+e^- \rightarrow Y \rightarrow \pi^+\pi^- J/\psi$ and $\pi^+\pi^-\psi(2S)$ ($Y = Y(4260)$, $Y(4660)$) processes, events in $\pi^+\pi^-$ mass spectra tend to accumulate at the $f_0(980)$ nominal mass, which has an $s\bar{s}$ component. Thus, it is natural to search for Y states with a $(c\bar{s})(\bar{c}s)$ quark component. As mentioned in Ref. [21], bound states of $D_s\bar{D}_s$ mesons, e.g., $D_s\bar{D}_{s1}(2536)$, can appear as a result of $f_0(980)$ exchange. Unfortunately, open-charmed-strange production associated with these Y states has not yet been observed.

In this Letter, we perform an exclusive cross section measurement of $e^+e^- \rightarrow D_s^+ D_{s1}(2536)^- (D_{s1}(2536)^- \rightarrow \bar{D}^{*0} K^- / D^{*-} K_S^0)$ as a function of center-of-mass (C.M.) energy from the $D_s^+ D_{s1}(2536)^-$ mass threshold to

5.59 GeV via initial-state radiation (ISR) [22]. In this process, a charmoniumlike state decaying to $D_s^+ D_{s1}(2536)^-$ is observed for the first time. The data used in this analysis corresponds to 921.9 fb^{-1} of integrated luminosity at C.M. energies of 10.52, 10.58, and 10.867 GeV collected by the Belle detector [23] at the KEKB asymmetric-energy e^+e^- collider [24, 25].

We use PHOKHARA [26] to generate signal Monte Carlo (MC) events, determine the detector efficiency, and optimize selection criteria for signal events. Generic MC samples of $\Upsilon(4S) \rightarrow B^+B^-/B^0\bar{B}^0$, $\Upsilon(5S) \rightarrow B_s^{(*)}\bar{B}_s^{(*)}$, and $e^+e^- \rightarrow q\bar{q}$ ($q = u, d, s, c$) at $\sqrt{s} = 10.52, 10.58,$ and 10.867 GeV with four times the luminosity of data are used to study possible backgrounds.

We fully reconstruct the ISR photon γ_{ISR} , D_s^+ , and K^-/K_S^0 , but do not reconstruct the \bar{D}^{*0}/D^{*-} . Since the \bar{D}^{*0}/D^{*-} decays are not reconstructed, the detector efficiency for the $e^+e^- \rightarrow D_s^+ D_{s1}(2536)^- (\rightarrow \bar{D}^{*0} K^- / D^{*-} K_S^0)$ process is greatly improved. For the measurement of the $e^+e^- \rightarrow D_s^+ D_{s1}(2536)^-$ cross section, we determine the invariant mass spectrum of $D_s^+ D_{s1}(2536)^- (M(D_s^+ D_{s1}(2536)^-))$, which is equivalent to the mass recoiling against γ_{ISR} ($M_{\text{rec}}(\gamma_{\text{ISR}})$). Here, $M_{\text{rec}}(\gamma_{\text{ISR}})$ is calculated using $M_{\text{rec}}(\gamma_{\text{ISR}}) = \sqrt{(P_{\text{C.M.}} - P_{\gamma_{\text{ISR}}})^2}$, where $P_{\text{C.M.}}$ and $P_{\gamma_{\text{ISR}}}$ are the four-momenta of the initial e^+e^- system and the ISR photon, respectively. However, the energy resolution of γ_{ISR} is very poor due to its high energy. We constrain the recoil mass of the $\gamma_{\text{ISR}} D_s^+ K^- / \gamma_{\text{ISR}} D_s^+ K_S^0$ to the nominal mass of the \bar{D}^{*0}/D^{*-} meson [27] to improve the resolution for the ISR photon in the events within the \bar{D}^{*0}/D^{*-} signal region. Before applying the mass constraint, the mass resolution of the $M(D_s^+ D_{s1}(2536)^-)$ system is about $180 \text{ MeV}/c^2$. As a result of the constraint, the mass resolution is significantly improved, to about $5 \text{ MeV}/c^2$.

The D_s^+ candidates are reconstructed using eight decay modes: $\phi\pi^+$, $\bar{K}^*(892)^0 K^+$, $K_S^0 K^+$, $K^+ K^- \pi^+ \pi^0$, $K_S^0 \pi^0 K^+$, $K^*(892)^+ K_S^0$, $\eta\pi^+$, and $\eta'\pi^+$. We use the techniques of Ref. [28] to reconstruct particles such as photons, charged pions and kaons, and K_S^0 . The ϕ , $\bar{K}^*(892)^0$, and $K^*(892)^+$ candidates are reconstructed in the $K^+ K^-$, $K^- \pi^+$, and $K_S^0 \pi^+$ decay modes. The invariant masses of the K_S^0 , ϕ , $\bar{K}^*(892)^0$, and $K^*(892)^+$ candidates are required to be within 10, 10, 50, and 50 MeV/c^2 of the corresponding nominal masses [27] (>95% signal events are retained), respectively.

The most energetic ISR photon is required to have energy greater than 3 GeV in the e^+e^- C.M. frame. Pairs of photons are combined to form π^0 candidates. The energies of the photons from π^0 are required to be greater than 50 MeV in the calorimeter barrel and 100 MeV in the calorimeter endcaps [29] in the laboratory frame. The η candidates are reconstructed via $\gamma\gamma$ and $\pi^+\pi^-\pi^0$ decay modes. Photon candidates from $\eta \rightarrow \gamma\gamma$ are required to have energies greater than 100 MeV in the laboratory

frame. The reconstructed η candidates are then combined with $\pi^+\pi^-$ pairs to form η' candidates. The mass windows applied for π^0 , $\eta \rightarrow \gamma\gamma$, $\eta \rightarrow \pi^+\pi^-\pi^0$, and η' candidates are $\pm 12, \pm 20, \pm 10,$ and $\pm 10 \text{ MeV}/c^2$, which are within approximately 2.5σ of the corresponding meson nominal masses [27]. After applying the mass window requirements, mass-constrained fits are applied to the π^0 , η , and η' candidates to improve their momentum resolutions.

Before calculation of the D_s^+ candidate mass, a fit to a common vertex is performed for charged tracks in the D_s^+ candidate. After the application of the above requirements, D_s^+ signals are clearly observed. We define the D_s^+ signal region as $|M(D_s^+) - m_{D_s^+}| < 12 \text{ MeV}/c^2$ ($\sim 2.0\sigma$). Here and throughout the text, m_i represents the nominal mass of particle i [27]. To improve the momentum resolution of the D_s^+ meson candidate, a mass-constrained fit to the D_s^+ nominal mass [27] is performed. The D_s^+ mass sideband regions are defined as $1912.34 < M(D_s^+) < 1936.34 \text{ MeV}/c^2$ and $2000.34 < M(D_s^+) < 2024.34 \text{ MeV}/c^2$, which are twice as wide as the signal region. The D_s^+ candidates from the sidebands are also constrained to the central mass values in the defined D_s^+ sideband regions. The D_s^+ candidate with the smallest χ^2 from the D_s^+ mass fit is kept. Besides the selected ISR photon and D_s^+ , we require at least one additional K^- or K_S^0 candidate in the event, and retain all the combinations (the fraction of events with multiple candidates is 1.7%).

Figure 1(a) shows the sum of the recoil mass spectra against the $\gamma_{\text{ISR}} D_s^+ K^-$ and $\gamma_{\text{ISR}} D_s^+ K_S^0$ systems after requiring the events within the $D_{s1}(2536)^-$ signal region (see below) in data. Due to the poor recoil mass resolution, the \bar{D}^{*0}/D^{*-} signal is very wide. The \bar{D}^{*0}/D^{*-} signal component is modeled using a Gaussian function convolved with a Novosibirsk function [30] derived from the signal MC samples, while the combinatorial backgrounds are described by a second-order polynomial. The solid line is the total fit and the \bar{D}^{*0}/D^{*-} signal yield is 275 ± 32 . We define an asymmetric requirement of $-200 < M_{\text{rec}}(\gamma_{\text{ISR}} D_s^+ K^- / K_S^0) - m_{\bar{D}^{*0}/D^{*-}} < 400 \text{ MeV}/c^2$ for the \bar{D}^{*0}/D^{*-} signal region. Hereinafter the \bar{D}^{*0}/D^{*-} mass constraint is applied for events in the \bar{D}^{*0}/D^{*-} signal region to improve mass resolution.

The recoil mass spectrum against the $\gamma_{\text{ISR}} D_s^+$ system after requiring the events within \bar{D}^{*0}/D^{*-} signal region is shown in Fig. 1(b). A clear $D_{s1}(2536)^-$ signal is observed. The signal shape is described by a double Gaussian function (all the parameters are fixed to those from a fit to the MC simulated distribution), and a threshold function is used for the backgrounds. The threshold function is $(M_{\text{rec}} - x_{\text{thr}}) \alpha e^{[\beta_1(M_{\text{rec}} - x_{\text{thr}}) + \beta_2(M_{\text{rec}} - x_{\text{thr}})^2]}$, where M_{rec} is the recoil mass of the $\gamma_{\text{ISR}} D_s^+$; the parameters α , β_1 , and β_2 are free; the threshold parameter x_{thr} is fixed from generic MC simulations. The fit yields $254 \pm 36 D_{s1}(2536)^-$ signal events as shown in Fig. 1(b). We define the $D_{s1}(2536)^-$ signal region as

$|M_{\text{rec}}(\gamma_{\text{ISR}}D_s^+) - m_{D_{s1}(2536)^-}| < 8 \text{ MeV}/c^2$ ($\sim 2.5\sigma$), and sideband regions as shown by blue dashed lines, which are three times as wide as the signal region. To estimate the signal significance of the $D_{s1}(2536)^-$, we compute $\sqrt{-2\ln(\mathcal{L}_0/\mathcal{L}_{\text{max}})}$ [31], where \mathcal{L}_0 and \mathcal{L}_{max} are the maximized likelihoods without and with the $D_{s1}(2536)^-$ signal, respectively. The statistical significance of the $D_{s1}(2536)^-$ signal is 8σ .

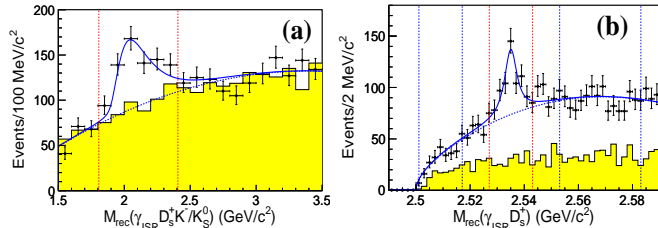


FIG. 1: (a) The recoil mass spectrum against the $\gamma_{\text{ISR}}D_s^+K^-/K_S^0$ system before applying the \bar{D}^{*0}/D^{*-} mass constraint. The yellow histogram shows the normalized $D_{s1}(2536)^-$ mass sidebands (see below). The red dashed lines show the required \bar{D}^{*0}/D^{*-} signal region. (b) The recoil mass spectrum against the $\gamma_{\text{ISR}}D_s^+$ system in data. The yellow histogram shows the normalized D_s^+ mass sidebands. The red dashed lines show the required $D_{s1}(2536)^-$ signal region, and the blue dashed lines show the $D_{s1}(2536)^-$ mass sidebands.

The $D_s^+D_{s1}(2536)^-$ invariant mass distribution is shown in Fig. 2(a). There is a significant peak around $4626 \text{ MeV}/c^2$, while no structure is seen in the normalized $D_{s1}(2536)^-$ mass sidebands shown as the yellow histogram. In addition, no peaking background is found in the $D_s^+D_{s1}(2536)^-$ mass distribution from generic MC samples. We therefore interpret the peak in the data as evidence for an exotic charmoniumlike state decaying into $D_s^+D_{s1}(2536)^-$, called $Y(4626)$ hereafter.

One possible background, which is not included in the $D_{s1}(2536)^-$ mass sidebands is from $e^+e^- \rightarrow D_s^{*+}(\rightarrow D_s^+\gamma)D_{s1}(2536)^-$, where the photon from the D_s^{*+} remains undetected. To estimate such a background contribution, we measure this process with the data following the same procedure as used for the signal process. We require an extra photon with $E_\gamma > 50 \text{ MeV}$ in the barrel or $E_\gamma > 100 \text{ MeV}$ in the endcaps to combine with the D_s^+ to form the D_s^{*+} candidate. The mass and vertex fits are applied to the D_s^{*+} candidates to improve their momentum resolution. In events with multiple candidates, the best candidate is chosen using the lowest χ^2 value from the mass-constrained fit. The same \bar{D}^{*0}/D^{*-} signal region requirement on $M_{\text{rec}}(\gamma_{\text{ISR}}D_s^{*+}K^-/K_S^0)$ and the \bar{D}^{*0}/D^{*-} mass constraint are applied as before in $e^+e^- \rightarrow D_s^+D_{s1}(2536)^-$. In the recoil mass spectrum of the $\gamma_{\text{ISR}}D_s^{*+}$ an excess of events is observed in the $D_{s1}(2536)^-$ signal region.

After requiring the $D_s^+K^-/K_S^0$ mass to be within the $D_{s1}(2536)^-$ signal region, the $D_s^{*+}D_{s1}(2536)^-$

invariant mass distribution is shown in Fig. 2(b). Note that the $e^+e^- \rightarrow D_s^+D_{s1}(2536)^-$ is a source of backgrounds for the $e^+e^- \rightarrow D_s^{*+}D_{s1}(2536)^-$ when the D_s^+ candidates are combined with soft photons to form D_s^{*+} candidates. From Fig. 2(b), no obvious structure is observed. The normalized contribution from $e^+e^- \rightarrow D_s^{*+}D_{s1}(2536)^-$ to $e^+e^- \rightarrow D_s^+D_{s1}(2536)^-$ is the cyan shaded histogram which is shown in Fig. 2(a), and which is normalized to correspond to $N_{D_s^+D_{s1}(2536)^-}^{\text{obs}} - \varepsilon_{D_s^+D_{s1}(2536)^-} / \varepsilon_{D_s^{*+}D_{s1}(2536)^-}$ events. Here, $N_{D_s^{*+}D_{s1}(2536)^-}^{\text{obs}}$ is the yield of $e^+e^- \rightarrow D_s^{*+}D_{s1}(2536)^-$ signal events in each $M(D_s^{*+}D_{s1}(2536)^-)$ bin in data after subtracting the normalized $D_{s1}(2536)^-$ sidebands and the $e^+e^- \rightarrow D_s^+D_{s1}(2536)^-$ background contribution, and $\varepsilon_{D_s^+D_{s1}(2536)^-}$ and $\varepsilon_{D_s^{*+}D_{s1}(2536)^-}$ are the reconstruction efficiencies for $e^+e^- \rightarrow D_s^+D_{s1}(2536)^-$ and $e^+e^- \rightarrow D_s^{*+}D_{s1}(2536)^-$, respectively, and the ratio of efficiencies is (1.00 ± 0.02) . The yield of $D_s^{*+}D_{s1}(2536)^-$ after the background subtraction for the whole region in Fig. 2(b) is (11.6 ± 3.6) . A similar method is applied to estimate the background contribution from $e^+e^- \rightarrow D_s^+D_{s1}(2536)^-$ to $e^+e^- \rightarrow D_s^{*+}D_{s1}(2536)^-$.

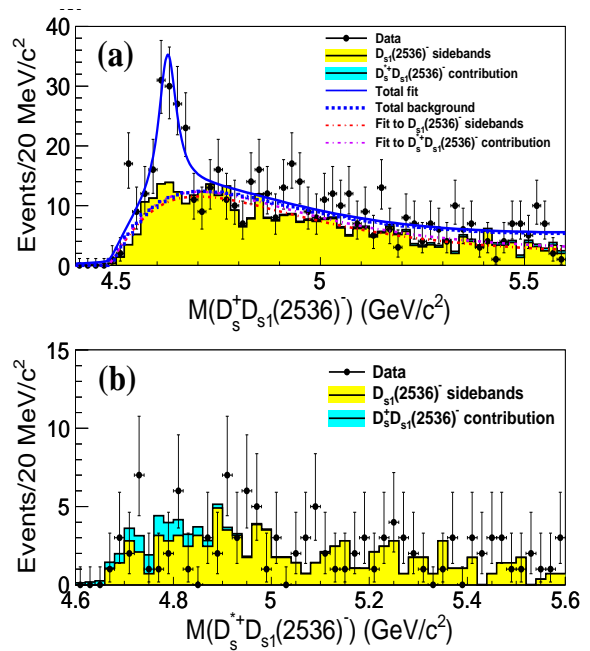


FIG. 2: (a) The $D_s^+D_{s1}(2536)^-$ invariant mass spectrum for $e^+e^- \rightarrow D_s^+D_{s1}(2536)^-$. (b) The $D_s^{*+}D_{s1}(2536)^-$ invariant mass spectrum for $e^+e^- \rightarrow D_s^{*+}D_{s1}(2536)^-$. All the components including those from the fit to the $D_s^+D_{s1}(2536)^-$ invariant mass spectrum are indicated in the labels and described in the text. Note that the cyan shaded histograms in the top/bottom show the $D_s^+D_{s1}(2536)^-/D_s^{*+}D_{s1}(2536)^-$ invariant mass spectrum from $D_s^+D_{s1}(2536)^-/D_s^{*+}D_{s1}(2536)^-$ background contribution after applying the requirements to reconstruct $e^+e^- \rightarrow D_s^+D_{s1}(2536)^-/e^+e^- \rightarrow D_s^{*+}D_{s1}(2536)^-$.

We perform an unbinned likelihood fit simultaneously to the $M(D_s^+ D_{s1}(2536)^-)$ distributions of all selected $D_{s1}(2536)^-$ signal candidates, the normalized $D_{s1}(2536)^-$ mass sidebands, and the $e^+e^- \rightarrow D_s^{*+} D_{s1}(2536)^-$ contribution. The following components are included in the fit to the $M(D_s^+ D_{s1}(2536)^-)$ distribution: a resonance signal, a non-resonant contribution, the $D_{s1}(2536)^-$ mass sidebands, and the $e^+e^- \rightarrow D_s^{*+} D_{s1}(2536)^-$ contribution. A Breit-Wigner (BW) function convolved with a Gaussian function (with its width fixed at 5.0 MeV/ c^2 according to the MC simulation), multiplied by an efficiency function that has a linear dependence on $M(D_s^+ D_{s1}(2536)^-)$ and the differential ISR effective luminosity [32] is taken as the signal shape. Here the BW formula used has the form [33]

$$BW(\sqrt{s}) = \frac{\sqrt{12\pi}\Gamma_{ee}\mathcal{B}_f\Gamma}{s - M^2 + iM\Gamma} \sqrt{\frac{\Phi_2(\sqrt{s})}{\Phi_2(M)}}, \quad (1)$$

where M is the mass of the resonance, Γ and Γ_{ee} are the total width and partial width to e^+e^- , $\mathcal{B}_f = \mathcal{B}(Y(4626) \rightarrow D_s^+ D_{s1}(2536)^-) \times \mathcal{B}(D_{s1}(2536)^- \rightarrow \bar{D}^{*0} K^-)$ is the product branching fraction of the $Y(4626)$ into the final state, and Φ_2 is the two-body decay phase space factor that increases smoothly from the mass threshold with \sqrt{s} . A two-body phase space form is also taken into account for the non-resonant contribution. The $D_{s1}(2536)^-$ mass sidebands and the $e^+e^- \rightarrow D_s^{*+} D_{s1}(2536)^-$ contribution are parameterized with threshold functions.

The fit results are shown in Fig. 2(a), where the solid blue curve is the best fit, the blue dotted curve is the sum of the backgrounds, the red dot-dashed curve is the fitted result to the normalized $D_{s1}(2536)^-$ mass sidebands, and the violet dot-dashed curve is for the $e^+e^- \rightarrow D_s^{*+} D_{s1}(2536)^-$ contribution. The yield of the $Y(4626)$ signal is 89^{+17}_{-16} . The statistical significance of the $Y(4626)$ signal is 6.5σ , calculated from the difference of the logarithmic likelihoods [31], $-2 \ln(\mathcal{L}_0/\mathcal{L}_{\max}) = 50.4$, where \mathcal{L}_0 and \mathcal{L}_{\max} are the maximized likelihoods without and with a signal component, respectively, taking into account the difference in the number of degrees of freedom ($\Delta\text{ndf} = 3$). The parameterization of the non-resonant contribution is the dominant systematic uncertainty for the estimate of the signal significance. Changing the two-body phase space form to a threshold function parameterized by $\sqrt{M - x_{\text{thr}}}$ or a two-body phase space form plus a threshold function, the $Y(4626)$ signal significance is reduced to 5.9σ . We take this value as the signal significance with systematic uncertainties included. The fitted mass and width for the $Y(4626)$ are $(4625.9^{+6.2}_{-6.0}(\text{stat.}) \pm 0.4(\text{syst.}))$ MeV/ c^2 and $(49.8^{+13.9}_{-11.5}(\text{stat.}) \pm 4.0(\text{syst.}))$ MeV, respectively. The value of $\Gamma_{ee} \times \mathcal{B}(Y(4626) \rightarrow D_s^+ D_{s1}(2536)^-) \times \mathcal{B}(D_{s1}(2536)^- \rightarrow \bar{D}^{*0} K^-)$ is obtained to be $(14.3^{+2.8}_{-2.6}(\text{stat.}) \pm 1.5(\text{syst.}))$ eV. The systematic uncertainties are discussed below.

The product of the $e^+e^- \rightarrow D_s^+ D_{s1}(2536)^-$ dressed

cross section (σ) [34] and the decay branching fraction $\mathcal{B}(D_{s1}(2536)^- \rightarrow \bar{D}^{*0} K^-)$ for each $D_s^+ D_{s1}(2536)^-$ mass bin from threshold to 5.59 GeV/ c^2 in steps of 20 MeV/ c^2 is computed as

$$\sigma(e^+e^- \rightarrow D_s^+ D_{s1}(2536)^-) \mathcal{B}(D_{s1}(2536)^- \rightarrow \bar{D}^{*0} K^-) = \frac{N_{\text{fit}}^{D_{s1}(2536)^-}}{d\mathcal{L} \times [\Sigma_i(\varepsilon_i^{\bar{D}^{*0} K^-} \times \mathcal{B}_i) + R_{\bar{D}^{*0} K^-}^{D^* K_S^0} \times \Sigma_i(\varepsilon_i^{D^* K_S^0} \times \mathcal{B}_i)]}, \quad (2)$$

where $N_{\text{fit}}^{D_{s1}(2536)^-}$, $d\mathcal{L}$, $\Sigma_i(\varepsilon_i^{\bar{D}^{*0} K^-} \times \mathcal{B}_i)$, and $\Sigma_i(\varepsilon_i^{D^* K_S^0} \times \mathcal{B}_i)$ are the yields of fitted $D_{s1}(2536)^-$ signal events after subtracting the $e^+e^- \rightarrow D_s^{*+} D_{s1}(2536)^-$ background contribution in data, the effective luminosity [32], the sums of the product of the reconstruction efficiency and branching fraction for each D_s^+ decay mode (i) in $D_{s1}(2536)^- \rightarrow \bar{D}^{*0} K^-$ and $D_{s1}(2536)^- \rightarrow D^* K_S^0$, in each $D_s^+ D_{s1}(2536)^-$ mass bin, respectively; $R_{\bar{D}^{*0} K^-}^{D^* K_S^0} = \mathcal{B}(D_{s1}(2536)^- \rightarrow D^* K_S^0)/\mathcal{B}(D_{s1}(2536)^- \rightarrow \bar{D}^{*0} K^-) = 0.425 \pm 0.06$ is taken from Ref. [27]. The values used to calculate $\sigma(e^+e^- \rightarrow D_s^+ D_{s1}(2536)^-) \mathcal{B}(D_{s1}(2536)^- \rightarrow \bar{D}^{*0} K^-)$ are summarized in the Supplemental Material [36]. In the fit to the recoil mass spectrum of $\gamma_{\text{ISR}} D_s^+$ combinations in each $D_s^+ D_{s1}(2536)^-$ mass bin, the $D_{s1}(2536)^-$ signal shape is fixed to that from the overall fit, as shown by the blue solid curve in Fig. 1, and a threshold function is used for the backgrounds. The resulting $\sigma(e^+e^- \rightarrow D_s^+ D_{s1}(2536)^-) \times \mathcal{B}(D_{s1}(2536)^- \rightarrow \bar{D}^{*0} K^-)$ value as a function of $M(D_s^+ D_{s1}(2536)^-)$ is shown in Fig. 3 with the statistical and systematic uncertainties (discussed below) summed in quadrature.

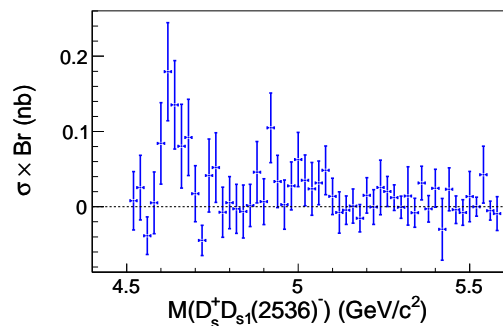


FIG. 3: The product of the $e^+e^- \rightarrow D_s^+ D_{s1}(2536)^-$ cross section and branching fraction $\mathcal{B}(D_{s1}(2536)^- \rightarrow \bar{D}^{*0} K^-)$ as a function of $M(D_s^+ D_{s1}(2536)^-)$; here the statistical and systematic uncertainties are summed in quadrature.

The sources of systematic uncertainties for the cross section measurement include detection-efficiency-related uncertainties, branching fractions of the intermediate states, fit uncertainty, resonance parameters, the MC event generator, $e^+e^- \rightarrow D_s^{*+} D_{s1}(2536)^-$ background contribution as well as the integrated luminosity. The detection-efficiency-related uncertainties include those

for tracking efficiency (0.35%/track), particle identification efficiency (1.1%/kaon and 0.9%/pion), K_S^0 selection efficiency (1.4%) [37], π^0 reconstruction efficiency (2.25%/ π^0), and photon reconstruction efficiency (2.0%/photon). The above individual uncertainties from different D_s^+ decay channels are added linearly, weighted by the product of the detection efficiency and D_s^+ partial decay width. These uncertainties are summed in quadrature to obtain the final uncertainty related to the reconstruction efficiency. Uncertainties for D_s^+ decay branching fractions and $R_{\bar{D}^{*0}K^-}^{D^{*-}K_S^0}$ are taken from Ref. [27]; the final uncertainties on the D_s^+ partial decay widths are summed in quadrature over the eight D_s^+ decay modes weighted by the product of the efficiency and the D_s^+ partial decay width. Systematic uncertainties associated with the fitting procedure are estimated by changing the order of the background polynomial and the range of the fit. The deviations from nominal fit results are taken as systematic uncertainties. Changing the values of mass and width of $D_{s1}(2536)^-$ by 1σ [27] in each $M(D_s^+D_{s1}(2536)^-)$ bin has no effect on the fits. Thus, the uncertainty from the resonance parameters can be neglected. The PHOKHARA generator calculates the ISR-photon radiator function with 0.1% accuracy [26]. The uncertainty attributed to the generator can also be neglected.

By fitting the $D_{s1}(2536)^-$ mass spectrum in each $M(D_s^+D_{s1}(2536)^-)$ bin for $e^+e^- \rightarrow D_s^{*+}D_{s1}(2536)^-$, we find the signal yields are less than 1. In addition, the $D_{s1}(2536)^-$ signal from the $e^+e^- \rightarrow D_s^{*+}D_{s1}(2536)^-$ contribution has a much poorer mass resolution according to MC simulation. Therefore, the systematic uncertainty associated with the $e^+e^- \rightarrow D_s^{*+}D_{s1}(2536)^-$ contribution is neglected. The total luminosity is determined to 1.4% precision using wide-angle Bhabha scattering events. All the uncertainties are summarized in Table I. Assuming all the sources are independent, we sum them in quadrature to obtain the total systematic uncertainties.

TABLE I: Summary of the absolute systematic uncertainties (σ_{sys}) on the product of $e^+e^- \rightarrow D_s^+D_{s1}(2536)^-$ cross section and the decay branching fraction $\mathcal{B}(D_{s1}(2536)^- \rightarrow \bar{D}^{*0}K^-)$ for different $M(D_s^+D_{s1}(2536)^-)$ bins.

Source	σ_{sys} (pb)
Detection efficiency	0.0 – 8.1
Branching fractions	0.0 – 7.4
Fit uncertainty	0.5 – 36.2
Luminosity	0.0 – 2.5
Quadratic Sum	0.6 – 36.3

The following systematic uncertainties on the mea-

sured mass and width for the $Y(4626)$, and the $\Gamma_{ee} \times \mathcal{B}(Y(4626) \rightarrow D_s^+D_{s1}(2536)^-) \times \mathcal{B}(D_{s1}(2536)^- \rightarrow \bar{D}^{*0}K^-)$ are considered. MC simulation is known to reproduce the resolution of mass peaks within 10% over a large number of different systems. The resultant systematic uncertainty in the width and $\Gamma_{ee} \times \mathcal{B}(Y(4626) \rightarrow D_s^+D_{s1}(2536)^-) \times \mathcal{B}(D_{s1}(2536)^- \rightarrow \bar{D}^{*0}K^-)$ from this source is 0.3 MeV and 0.1 eV. By changing the non-resonant background shape to a threshold function or to the sum of a two-body phase space form and a threshold function, the differences of 0.3 MeV/ c^2 and 3.9 MeV in the measured mass and width, and 1.3 eV for the $\Gamma_{ee} \times \mathcal{B}(Y(4626) \rightarrow D_s^+D_{s1}(2536)^-) \times \mathcal{B}(D_{s1}(2536)^- \rightarrow \bar{D}^{*0}K^-)$, respectively, are taken as systematic uncertainties. The uncertainty in the efficiency correction from detection efficiency, branching fractions of the intermediate states, and the integrated luminosity is 4.9%. Changing the efficiency function by 4.9% gives a 0.1 MeV/ c^2 change on the mass, 0.2 MeV on the width, and 0.7 eV on the product $\Gamma_{ee} \times \mathcal{B}(Y(4626) \rightarrow D_s^+D_{s1}(2536)^-) \times \mathcal{B}(D_{s1}(2536)^- \rightarrow \bar{D}^{*0}K^-)$. Finally, the total systematic uncertainties on the $Y(4626)$ mass, width, and $\Gamma_{ee} \times \mathcal{B}(Y(4626) \rightarrow D_s^+D_{s1}(2536)^-) \times \mathcal{B}(D_{s1}(2536)^- \rightarrow \bar{D}^{*0}K^-)$ are 0.4 MeV/ c^2 , 4.0 MeV, and 1.5 eV, respectively.

In summary, the product of the $e^+e^- \rightarrow D_s^+D_{s1}(2536)^-$ cross section and the decay branching fraction $\mathcal{B}(D_{s1}(2536)^- \rightarrow \bar{D}^{*0}K^-)$ is measured over the C.M. energy range from the $D_s^+D_{s1}(2536)^-$ mass threshold to 5.59 GeV for the first time. We observe the first vector charmoniumlike state decaying to a charmed-antistrange and anticharmed-strange meson pair $D_s^+D_{s1}(2536)^-$ with a signal significance of 5.9σ with systematic uncertainties included. The measured mass and width are $(4625.9_{-6.0}^{+6.2}(\text{stat.}) \pm 0.4(\text{syst.}))$ MeV/ c^2 and $(49.8_{-11.5}^{+13.9}(\text{stat.}) \pm 4.0(\text{syst.}))$ MeV, respectively, which are close to those of the $Y(4660)$ state [27]. The $\Gamma_{ee} \times \mathcal{B}(Y(4626) \rightarrow D_s^+D_{s1}(2536)^-) \times \mathcal{B}(D_{s1}(2536)^- \rightarrow \bar{D}^{*0}K^-)$ is obtained to be $(14.3_{-2.6}^{+2.8}(\text{stat.}) \pm 1.5(\text{syst.}))$ eV.

We thank the KEKB group for excellent operation of the accelerator; the KEK cryogenics group for efficient solenoid operations; and the KEK computer group, the NII, and PNNL/EMSL for valuable computing and SINET5 network support. We acknowledge support from MEXT, JSPS and Nagoya's TLPRC (Japan); ARC (Australia); FWF (Austria); NSFC and CCEPP (China); MSMT (Czechia); CZF, DFG, EXC153, and VS (Germany); DST (India); INFN (Italy); MOE, MSIP, NRF, RSRI, FLRFAS project, GSDC of KISTI and KREONET/GLORIAD (Korea); MNiSW and NCN (Poland); MSHE, Agreement 14.W03.31.0026 (Russia); ARRS (Slovenia); IKERBASQUE (Spain); SNSF (Switzerland); MOE and MOST (Taiwan); and DOE and NSF (USA).

-
- [1] G. Pakhlova *et al.* (Belle Collaboration), Phys. Rev. D **77**, 011103 (2008).
- [2] G. Pakhlova *et al.* (Belle Collaboration), Phys. Rev. Lett. **98**, 092001 (2007).
- [3] G. Pakhlova *et al.* (Belle Collaboration), Phys. Rev. Lett. **100**, 062001 (2008).
- [4] G. Pakhlova *et al.* (Belle Collaboration), Phys. Rev. D **80**, 091101 (2009).
- [5] G. Pakhlova *et al.* (Belle Collaboration), Phys. Rev. Lett. **101**, 172001 (2008).
- [6] G. Pakhlova *et al.* (Belle Collaboration), Phys. Rev. D **83**, 011101 (R) (2011).
- [7] M. Ablikim *et al.* (BESIII Collaboration), Phys. Rev. Lett. **120**, 132001 (2018).
- [8] B. Aubert *et al.* (BABAR Collaboration), Phys. Rev. D **76**, 111105 (2007).
- [9] B. Aubert *et al.* (BABAR Collaboration), Phys. Rev. D **79**, 092001 (2009).
- [10] P. del Amo Sanchez *et al.* (BABAR Collaboration), Phys. Rev. D **82**, 052004 (2010).
- [11] D. Cronin-Hennessy *et al.* (CLEO Collaboration), Phys. Rev. D **80**, 072001 (2009).
- [12] B. Aubert *et al.* (BABAR Collaboration), Phys. Rev. Lett. **95**, 142001 (2005).
- [13] M. Ablikim *et al.* (BESIII Collaboration), Phys. Rev. Lett. **100**, 102003 (2008).
- [14] T. E. Coan *et al.* (CLEO Collaboration), Phys. Rev. Lett. **96**, 162003 (2006).
- [15] C. Z. Yuan *et al.* (Belle Collaboration), Phys. Rev. Lett. **99**, 182004 (2007).
- [16] Z. Q. Liu *et al.* (Belle Collaboration), Phys. Rev. Lett. **110**, 252002 (2013).
- [17] M. Ablikim *et al.* (BESIII Collaboration), Phys. Rev. Lett. **118**, 092001 (2017).
- [18] B. Aubert *et al.* (BABAR Collaboration), Phys. Rev. Lett. **98**, 212001 (2007).
- [19] X. L. Wang *et al.* (Belle Collaboration), Phys. Rev. Lett. **99**, 142002 (2007).
- [20] M. Ablikim *et al.* (BESIII Collaboration), Phys. Rev. D **96**, 032004 (2017).
- [21] M. Karliner and J. L. Rosner, Nucl. Phys. A **954**, 365 (2016).
- [22] Throughout this analysis, for any given mode, the corresponding charge-conjugate mode is implied.
- [23] A. Abashian *et al.* (Belle Collaboration), Nucl. Instrum. Methods Phys. Res. Sect. A **479**, 117 (2002); also see Section 2 in J. Brodzicka *et al.*, Prog. Theor. Exp. Phys. **2012**, 04D001 (2012).
- [24] S. Kurokawa and E. Kikutani, Nucl. Instrum. Methods Phys. Res. Sect. A **499**, 1 (2003), and other papers included in this Volume.
- [25] T. Abe *et al.*, Prog. Theor. Exp. Phys. **2013**, 03A001 (2013) and references therein.
- [26] G. Rodrigo, H. Czyż, J. H. Kühn, and M. Szopa, Eur. Phys. J. C **24** 71 (2002) .
- [27] M. Tanabashi *et al.* (Particle Data Group), Phys. Rev. D **98**, 010001 (2018).
- [28] S. Jia *et al.* (Belle Collaboration), Phys. Rev. D **98**, 092015 (2018).
- [29] H. Ikeda *et al.* (Belle Collaboration), Nucl. Instrum. Methods Phys. Res. Sect. A **441**, 401 (2000).
- [30] The Novosibirsk function is defined as $f(x) = \exp[-\frac{1}{2}(\ln^2(1 + \Lambda(x - x_0))/\tau^2 + \tau^2)]$ with $\Lambda = \sinh(\tau\sqrt{\ln 4})/(\sigma\sqrt{\ln 4})$. The parameters represent the mean (x_0), the width (σ) and the tail asymmetry (τ).
- [31] S. S. Wilks, Ann. Math. Stat. **9**, 60 (1938).
- [32] E. A. Kuraev and V. S. Fadin, Sov. J. Nucl. Phys. **41**, 466 (1985) [Yad. Fiz. **41**, 733 (1985)].
- [33] X. Y. Gao, C. P. Shen, and C. Z. Yuan, Phys. Rev. D **95**, 092007 (2017).
- [34] The dressed cross section is $\sigma = \sigma^B/|1 - \Pi|^2$, where σ^B is the Born cross section, and $|1 - \Pi|^2 = 0.94$ is the vacuum polarization factor [35].
- [35] S. Actis *et al.*, Eur. Phys. J. C **66**, 585 (2010).
- [36] See Supplemental Material for a summary of the number of effective luminosity, the total reconstruction efficiency, the number of fitted signal events, and the product of the dressed cross section and the decay branching fraction $\sigma(e^+e^- \rightarrow D_s^+ D_{s1}(2536)^-) \times \mathcal{B}(D_{s1}(2536)^- \rightarrow \bar{D}^{*0} K^-)$ in each $D_s^+ D_{s1}(2536)^-$ mass bin.
- [37] N. Dash *et al.* (Belle Collaboration), Phys. Rev. Lett. **119**, 171801 (2017).

Supplemental Material

The product of cross section and decay branching fraction

$$\sigma(e^+e^- \rightarrow D_s^+ D_{s1}(2536)^-) \times \mathcal{B}(D_{s1}(2536)^- \rightarrow \bar{D}^{*0} K^-)$$

The number of effective luminosity $d\mathcal{L}$, the total reconstruction efficiency ε_{tot} , the number of fitted signal events N^{fit} , and the product of dressed cross section and decay branching fraction $\sigma \times \mathcal{B}$ in each $D_s^+ D_{s1}(2536)^-$ mass bin are summarized in Table II. The ε_{tot} equals to $[\Sigma_i(\varepsilon_i^{\bar{D}^{*0} K^-} \times \mathcal{B}_i) + R_{\bar{D}^{*0} K^-}^{D^{*-} K_S^0} \times \Sigma_i(\varepsilon_i^{D^{*-} K_S^0} \times \mathcal{B}_i)]$, where $\Sigma_i(\varepsilon_i^{\bar{D}^{*0} K^-} \times \mathcal{B}_i)$ and $\Sigma_i(\varepsilon_i^{D^{*-} K_S^0} \times \mathcal{B}_i)$ are the sums of the product of reconstruction efficiency and branching fraction for each D_s^+ decay mode (i) in $D_{s1}(2536)^- \rightarrow \bar{D}^{*0} K^-$ and $D_{s1}(2536)^- \rightarrow D^{*-} K_S^0$, and $R_{\bar{D}^{*0} K^-}^{D^{*-} K_S^0} = \mathcal{B}(D_{s1}(2536)^- \rightarrow D^{*-} K_S^0) / \mathcal{B}(D_{s1}(2536)^- \rightarrow \bar{D}^{*0} K^-) = (0.425 \pm 0.06)$.

TABLE II: The values of the product of dressed cross section and decay branching fraction $\sigma(e^+e^- \rightarrow D_s^+ D_{s1}(2536)^-) \times \mathcal{B}(D_{s1}(2536)^- \rightarrow \bar{D}^{*0} K^-)$ for the $e^+e^- \rightarrow D_s^+ D_{s1}(2536)^- + c.c.$ varying from $\sqrt{s} = 4.51$ to 5.59 GeV in a step of 0.02 GeV. For the N^{fit} , the uncertainty is statistical only, while for the dressed Born cross section σ , the first uncertainty is statistical and the second is systematic.

\sqrt{s} (GeV)	$d\mathcal{L}$ (pb^{-1})	N^{fit}	ε_{tot} (%)	$\sigma \times \mathcal{B}$ (pb)
4.52	87.6	0.9±4.3	0.128	8.0±38.8±0.7
4.54	88.2	2.9±4.9	0.129	25.4±42.8±2.7
4.56	88.8	-4.4±2.8	0.130	-38.5±24.3±5.7
4.58	89.4	0.6±4.8	0.130	5.2±40.9±3.2
4.60	90.0	9.9±6.0	0.131	84.2±50.9±18.4
4.62	90.6	21.4±7.3	0.132	179.4±61.5±21.4
4.64	91.3	16.4±6.5	0.132	135.3±54.0±23.1
4.66	91.9	9.8±6.1	0.133	80.4±50.0±24.7
4.68	92.5	11.4±5.4	0.134	92.1±43.5±25.8
4.70	93.1	2.2±4.5	0.134	17.4±35.6±11.0
4.72	93.8	-5.7±2.5	0.135	-44.7±19.6±4.1
4.74	94.4	5.3±5.7	0.135	41.5±44.5±19.4
4.76	95.0	6.7±5.8	0.136	52.1±44.9±11.2
4.78	95.7	-1.0±4.3	0.136	-7.3±33.3±1.1
4.80	96.3	0.7±4.5	0.137	5.4±33.7±7.7
4.82	97.0	-0.4±3.5	0.137	-2.7±26.4±19.0
4.84	97.7	-0.8±4.7	0.138	-6.3±34.6±6.9
4.86	98.3	0.2±3.6	0.138	1.7±26.6±9.2
4.88	99.0	6.3±5.6	0.139	45.9±40.7±3.6
4.90	99.7	0.9±3.5	0.139	6.8±25.3±16.9
4.92	100.4	14.7±6.3	0.140	104.9±45.0±10.8
4.94	101.1	4.8±4.8	0.140	33.6±33.6±8.8
4.96	101.7	0.4±4.5	0.141	2.8±31.1±10.1
4.98	102.4	4.0±4.6	0.141	27.7±31.5±4.5
5.00	103.1	9.1±5.0	0.141	62.7±34.1±11.5
5.02	103.9	5.2±4.6	0.142	35.1±30.9±13.7
5.04	104.6	3.5±4.3	0.142	23.8±29.3±19.2
5.06	105.3	4.8±4.3	0.142	31.7±29.0±2.2
5.08	106.0	7.3±4.8	0.143	48.4±31.4±8.0
5.10	106.7	2.1±3.2	0.143	13.8±21.0±12.0
5.12	107.5	-1.2±4.1	0.144	-7.6±26.8±6.1
5.14	108.2	-0.7±2.8	0.144	-4.5±17.9±6.2
5.16	109.0	0.1±3.5	0.144	0.9±22.4±4.1
5.18	109.7	-2.4±2.5	0.145	-15.3±15.6±9.2
5.20	110.5	2.4±3.7	0.145	15.1±23.2±4.4
5.22	111.3	-0.1±3.4	0.146	-0.4±21.1±9.2
5.24	112.0	4.2±4.2	0.146	25.6±25.9±25.4
5.26	112.8	3.4±3.3	0.146	20.3±20.0±1.5
5.28	113.6	2.0±2.8	0.147	12.2±16.7±2.8
5.30	114.4	-0.1±2.5	0.147	-0.7±14.7±0.6
5.32	115.2	2.4±4.0	0.148	14.3±23.7±30.6
5.34	116.0	-1.4±3.3	0.148	-8.0±19.2±1.5
5.36	116.8	5.5±3.8	0.149	31.5±22.0±3.7
5.38	117.6	-0.5±3.0	0.149	-2.8±17.1±4.4
5.40	118.5	4.4±3.7	0.150	24.5±21.0±13.9
5.42	119.3	-5.4±3.4	0.150	-30.0±19.0±36.3
5.44	120.1	4.2±4.1	0.151	23.2±22.8±17.1
5.46	121.0	-0.7±3.0	0.151	-3.9±16.4±8.3
5.48	121.9	-1.4±2.7	0.152	-7.7±14.5±8.9
5.50	122.7	2.5±3.2	0.153	13.6±17.1±28.7
5.52	123.6	0.0±2.4	0.153	0.0±12.6±0.8
5.54	124.5	8.2±5.2	0.154	42.6±27.0±26.6
5.56	125.4	-1.0±2.1	0.155	-5.2±10.7±6.7
5.58	126.3	-1.8±1.8	0.155	-9.1± 9.0±20.6